BNL-225306-2024-JAAM

# Three-Pole Wigglers at NSLS-II

M. Musardo

To be published in "Nuclear Instruments and Methods in Physics Research Section A: Accelerators, Spectrometers, Detectors and Associated Equipment"

February 2024

Photon Sciences

**Brookhaven National Laboratory**

**U.S. Department of Energy**

USDOE Office of Science (SC), Basic Energy Sciences (BES)

# DISCLAIMER

# Three-Pole Wigglers at NSLS-II

M. Musardo[a*], T. Tanabe[a], J. Rank[a], Y. Hidaka[a], D. Hidas[a], T. Corwin[a] and C. Kitegi[b]

[a]*National Synchrotron Light Source-II, Brookhaven National Laboratory, Upton, NY 11973, USA*

[b] *Synchrotron SOLEIL, L'Orme des Merisiers, 91190 Saint-Aubin, France*

**Abstract**

The National Synchrotron Light Source-II (NSLS-II) at Brookhaven National Lab (BNL) is a third-generation medium-energy storage ring with 3 GeV and sub-nm-rad horizontal emittance, equipped with a top-off capability of 500 mA. It is designed to deliver an extremely intense photon beam across a wide spectral range, from the far-infrared to the very hard X-ray region. This outstanding performance is achieved through a combination of bending magnets (BM), three-pole wigglers (3PW), and advanced insertion device (ID) sources. Six three-pole wigglers have been constructed at the NSLS-II IDs Lab. These devices are used to produce broadband radiation with lower angular power density and to monitor the electron beam emittance and energy spread. This paper describes the R&D activities focused on developing the required magnetic and mechanical designs, along with magnetic field optimization and the final magnetic measurement results. It also covers the spectral brightness, flux, power density, spatial and angular output properties of the 3PWs, including their commissioning results and their effects on the performance of the NSLS-II storage ring.

*Keyword*: Insertion Devices; Three-Pole Wiggler; Synchrotron Light Source; Magnetic Field Measurements; Particle Accelerator; Magnets

## 1. Introduction

The National Synchrotron Light Source-II (NSLS-II) at Brookhaven National Lab (BNL) is a high-brightness synchrotron light source facility operating at 3 GeV with a current of 500 mA. It is characterized by an electron beam with a horizontal emittance of approximately 0.68 nm·rad, an achievement made possible through the recent installation of a 4.3 T superconducting wiggler (SCW) [1]. As of September 2023, NSLS-II has eighteen fully operational insertion devices (IDs).

The NSLS-II electron storage ring consists of 30 double-bend achromat cells (DBA), featuring alternating straight sections with lengths ranging from 6.6 m to 9.3 m. Each straight section is achromatic and contains three quadrupoles at each end, which provide appropriate matching of the optic functions and tune advances in the straights to compensate for the strong influence of the insertion devices on the linear lattice [2]. To accommodate several three-pole wigglers as additional sources of hard X-rays, a 0.6 m long straight section was added at the downstream end of all 30 dispersion sections. To maintain the symmetry of these dispersion straights, corresponding vacant areas were also included at the upstream end of each section.

[*] Corresponding author. Tel.: +1-631-344-8821; fax: +1-631-344-4699; e-mail: musardo@bnl.gov.

The three-pole wigglers are used at NSLS-II as alternative broadband radiation sources for conventional bending magnet (BM) users. The bending magnets (0.4 T) employed at NSLS-II have a relatively low critical energy of 2.4 keV and they are excellent sources for low photon energies below 10 keV. But in order to meet the harder and stable X-ray source requirement, six 3PWs have been developed at NSLS-II. With a lower angular power density of 0.067 kW/mrad and a critical energy of 6.8 keV, they are excellent continuum hard X-ray sources up to 25 keV. Furthermore, these devices can be employed as diagnostic tools to monitor the NSLS-II electron beam emittance and energy spread as they are installed in a dispersive section [3].

## 2. NSLS-II three-pole wiggler mechanical and control system

Six 3PW units were developed in-house and seven, including the prototype unit, were installed into the NSLS-II storage ring. In this section, a detailed description of the mechanical design and control system of the device is presented. The permanent magnet cores of the 3PW are assembled within a holder designed to allow mechanical tuning using a system of adjustment screws while mapping the field. The longitudinal length is approximately 0.3 m. Two custom assembly fixtures are used to react against magnetic loads to assist with alignments during the construction of each core half and in mounting these halves to the L-shaped strong-back support [4]. The structure provides a C-frame of fixed gap construction (28.0 mm nominal between central poles) which is horizontally inserted into the electron beam using a stepper motor-driven ball screw. This single-axis stage allows for kinematic levelling beneath a fixed girder base shared with either of two large dipoles, depending on the beamline position. The 3PW stray field is negligible at the beam when in the fully retracted position. The entire assembly is mounted on a linear stage and can be moved approximately 200 mm in the transverse direction. The mechanical structure is shown in Fig. 1, and a 3D rendering is depicted in Fig. 2.

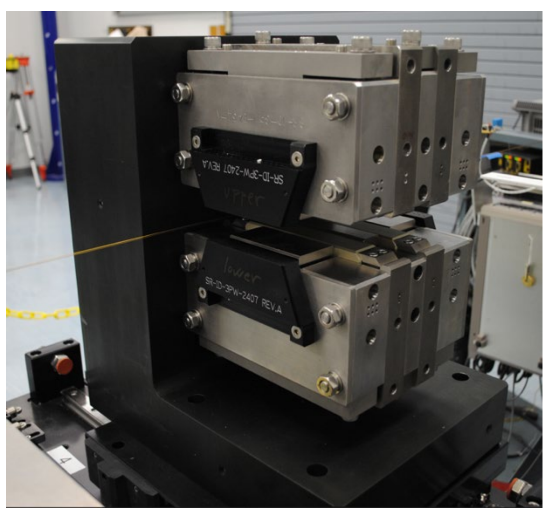

Figure 1: 3PW Mechanical structure.

A prototype, originally designed by Advanced Design Consulting USA, Inc. (ADC) and tuned in-house [5], now serves our beam diagnostics beamline, while six BNL-modified production units currently service other operational beamlines [6]. The production units rely on an absolute encoder and both inserted and extracted limit and kill switches for position feedback wired in a common signal cable (separate from the motor) to a Delta-Tau motor controller residing above on the mezzanine electronics rack. The same cable also carries an emergency stop and a homing switch for recovering from encoder positioning failures. Additionally, adjustable hard stops are in place to prevent the stage from derailing in case of a fault. A set of thermocouples measures the magnet core temperature to detect any potential overheating conditions. To protect the magnets and the thin-walled vacuum chamber extrusion from collisions, we first employ a set of chamber detection switches that trigger at ±250 μm misalignment in the elevation of the 3PW gap. Beyond these switches, there are protective soft brass nose pieces positioned just inside the pole gap. A Lexan guard clamps to the fixed chamber, shielding the gap from the strong permanent magnets in any position. The aluminium-anodized strongback includes several "cat's-eye" fiducial seats for ring alignment of the magnetic axis via a laser tracker.

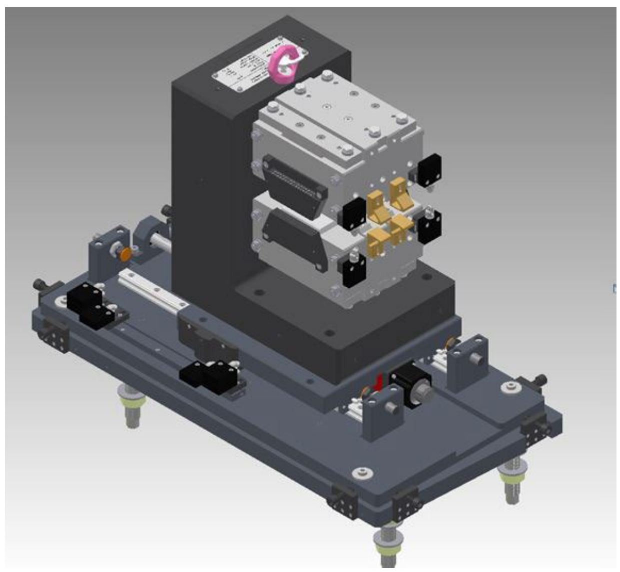

Figure 2: 3D rendering of the 3PW.

**3. Magnetic design and field optimization**

The 3PW utilizes a hybrid design consisting of four Neodymium Iron Boron (NdFeB) permanent magnets and six poles. The 3D model of the magnetic structure is displayed in Fig. 3. In this model, Z represents the longitudinal coordinate in the laboratory system, while X and Y denote the horizontal and vertical coordinates, respectively. The upper and lower magnet arrays consist of two NdFeB permanent magnets and three poles, positioned above and below the beam-pipe, respectively. The two central poles are made of Vanadium Permendur VACOFLUX50 (Vacuumschmelze GmbH & Co. KG), while the four side poles are made of low carbon iron steel. The design of the side poles was optimized to minimize their influence on the electron beam trajectory outside of the 3PW and to reduce emittance increase. To control costs, it was decided to use the same main magnets as those employed in NSLS-II damping wigglers. The magnet blocks used have a remanence of 1.24 T and an intrinsic coercivity of 24 kOe (VAC

863TP). The corners of the magnet blocks feature 5 mm deep cuts and are set back 1.5 mm relative to the central poles. Additionally, the poles have 2 mm deep 45° cuts in the transverse direction and 5 mm cuts at the ends facing the 3PW gap.

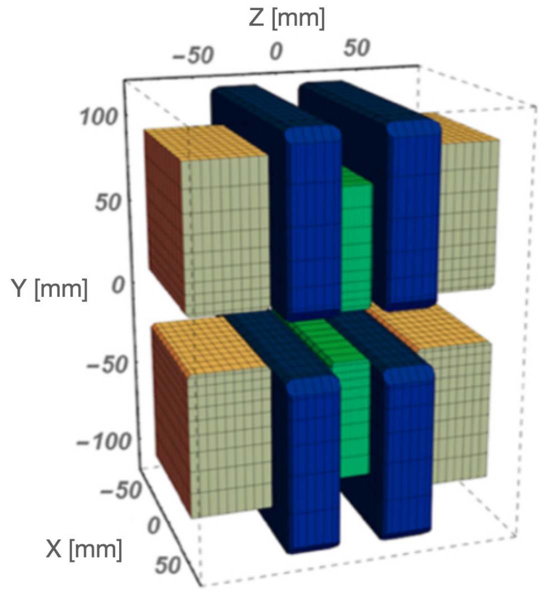


Figure 3: 3PW magnetic model optimized.

The Tab. 1 shows the optimized sizes of main magnet, central pole, and side pole, in order to achieve the required peak field at the gap center. The poles are supported by the magnet holders and can be horizontally and vertically adjusted using a set of shims placed between the magnets and poles.

Table 1: 3PW magnet dimensions

| | Main Magnet | Main Pole | Side Pole |
|---|---|---|---|
| Width | 150 mm | 110 mm | 40 mm |
| Height | 100 mm | 67 mm | 87 mm |
| Thickness | 28.9 mm | 23 mm | 45 mm |

The field profile has been designed to minimize the emittance degradation, while producing more than 2 mrad of fan angle above 1 T field. The increase in emittance, resulting from the insertion of a magnetic device generating the magnetic field $B_w$, can be described as follows [7]:

$$\epsilon_w[\mathrm{nm} \cdot \mathrm{rad}] = \frac{\epsilon_0[\mathrm{nm{\cdot}rad}]+0.12\times N\int (B_w[\mathrm{T}])^3 ds}{1+0.012\times N\int (B_w[\mathrm{T}])^2 ds}, \quad (1)$$

where $\varepsilon_0$ represents the initial emittance, which is 0.656 nm·rad with eighteen IDs and without any 3PWs, $N$ is the number of devices installed, and $B_w$ is the vertical field of the device. Based on this formula, adding seven 3PWs increases the emittance to 0.682 nm·rad. This is in good agreement with the result of an optical simulation using the computer code ELEGANT, which shows an emittance increase of 0.687 nm·rad.

In order to correct the field integral imperfection and compensate the multipole effects, a final magnetic tuning has been implemented by using small permanent magnet cylinders, which usually are called “Magic Fingers” [8]. The residual multipole components correction is performed by a fine vertical adjustment of small NdFeB magnets distributed along two-hole arrays on the horizontal axis, at both extremities of the 3PW. Their vertical displacement and magnetization direction can be individually adjusted to produce the desired integrated field distribution. This optimization was carried out by using “IDBuilder”, a genetic algorithm-based computer code for magnetic tuning of undulators [9]. Magic Fingers optimization was necessary for all 3PWs to ensure that the integral multipole coefficients are maintained within the NSLS-II specification requirements [10]. The Magic Finger holders consist of brackets mounted on both ends of the upper and lower magnet arrays on the upstream and downstream sides, totaling four brackets. There are two rows of holes for loading magnet 'pills' that make up the Magic Finger corrector magnets. One row corrects horizontal (skew) multipoles, and the other corrects vertical (normal) multipoles. The 2x16-holes array provides maximum correction with about 940 Magic Fingers. The magnets are loaded into the holder through the hole in the top, and the exposed end of the magnet is held with an aluminum spacer as it is moved up into the holder. This method prevents the magnet pill from flipping over if influenced by other already loaded magnets. Figures 4a and 4b show the residual multipole coefficients, normal and skew, respectively, after correction, using 23 magnetized cylinders with a remanent field of 1.2 T, diameter 3.5 mm, and height 2 mm.

Magnetic measurements have been performed by using a Hall-probe bench for field maps and a flip-coil for the field integral scans [11,12]. Measurement data provides information on the initial field integral, multipole, trajectory, peak field distribution and electron angle errors. Off-axis field integrals and local field measurements were performed to verify the basic design performance requirements. A peak field higher than 1 T and fan angle larger than 2 mrad were achieved for all devices. Figure 5a shows the measured field distribution of one unit, the peak field value is 1.1427 T.

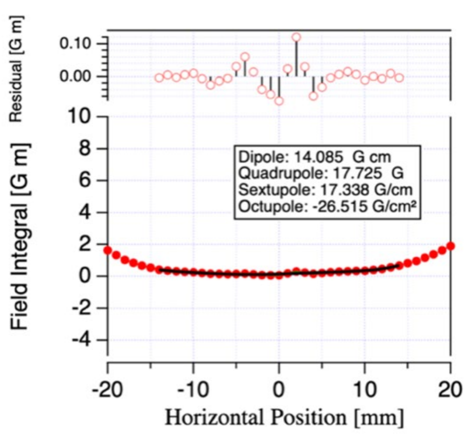


Figure 4a: Vertical field integral (solid red dots) and its 4th order polynomial fit (black line) as a function of the horizontal position. The resulting polynomial coefficients correspond to the normal multipole components. The plot includes residuals, illustrating the variances between each measured data point and the values predicted by the polynomial equation.

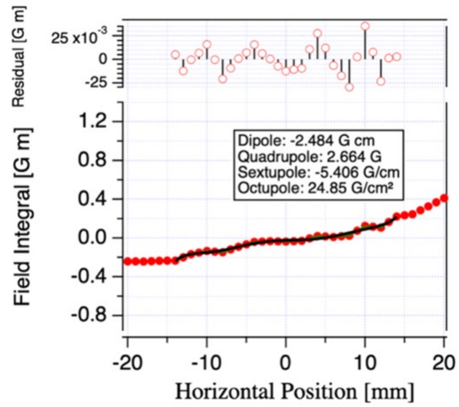


Figure 4b: Horizontal field integral (solid red dots) and its 4th order polynomial fit (black line) as a function of the horizontal position. The resulting polynomial coefficients correspond to the skew multipole components. The plot includes residuals, illustrating the variances between each measured data point and the values predicted by the polynomial equation.

Figure 5b shows the electron angle averaged on the 3PW centerline. The corresponding 3 GeV electron trajectory is shown in Fig. 6. Systematic measurements off-axis in the range ±10 mm were performed to estimate the maximum deflection of the horizontal and vertical trajectory. As shown in Fig. 6 the maximum displacement at the exit of the device is just few microns for both components as well as the maximum orbit deflection in the horizontal plane at Z = 0. Off-axis measurements clearly demonstrate the effectiveness of the correction on the trajectory.

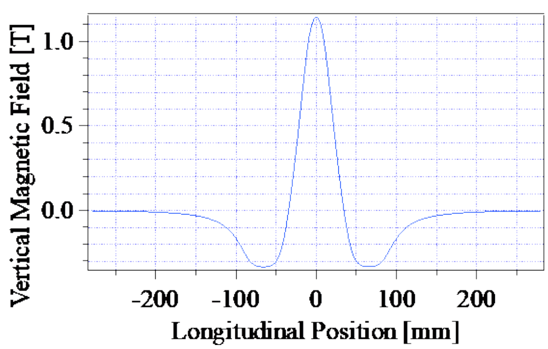


Figure 5a: Vertical magnetic field on-axis along the longitudinal axis.

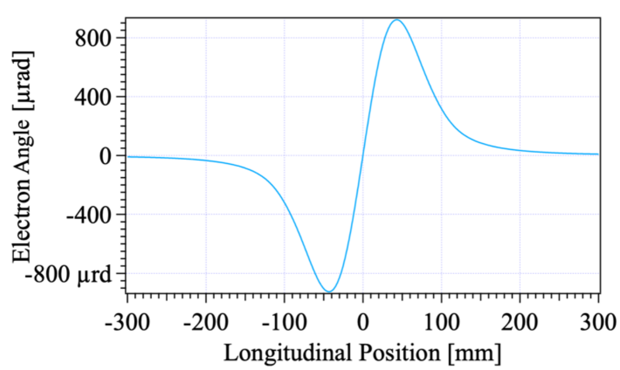


Figure 5b: Vertical electron angle over the length of the 3PW.

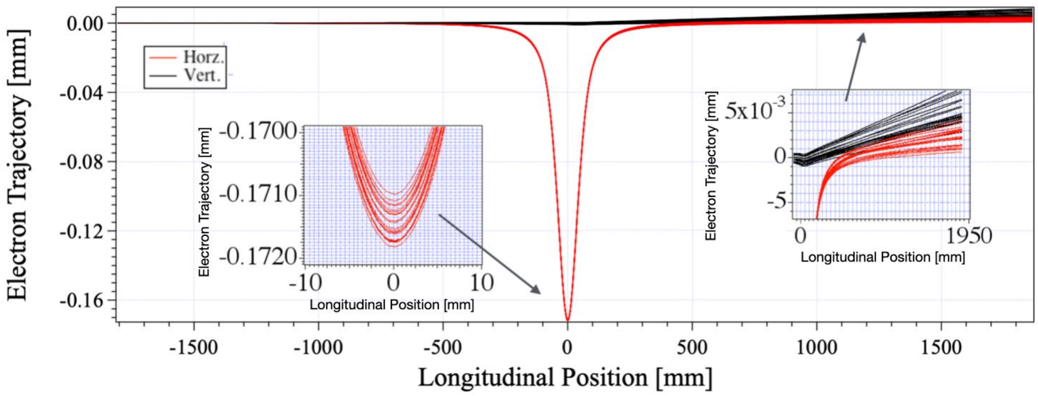


Figure 6: Horizontal (red line) and vertical (black line) electron trajectory off-axis measured at different transverse positions in the range ±10 mm.

Normal and skew multipole residual errors have been measured at the retracted position, which is located at 19.5 cm from the magnetic center of the device. The vertical field integral component is about -475 G cm, while the horizontal is 29 G cm constant over the entire measurement range. The multipole coefficients are illustrated in Tab. 2.

Table 2: Multipole components at retraced position magnet dimensions

| Multipole | Normal | Skew |
|---|---|---|
| Quadrupole | 6.8 G | -0.27 G |
| Sextupole | 14.57 G/cm | 3.53 G/cm |
| Octupole | -2.75 $G/cm^2$ | -1.39 $G/cm^2$ |

## 4. Spectral performance and commissioning results

The radiation properties of the 3PWs have been calculated using OSCARS, an open-source code for advanced radiation simulation [13]. Figure 7 shows a theoretical calculation of the spectral photon flux emitted by a 1.18 T 3PW, a 0.4 T dipole, a high-field superconducting wiggler (SCW70) with a period length of 70 mm., and a 1.85 T damping wiggler (DW) with a period length of 100 mm.

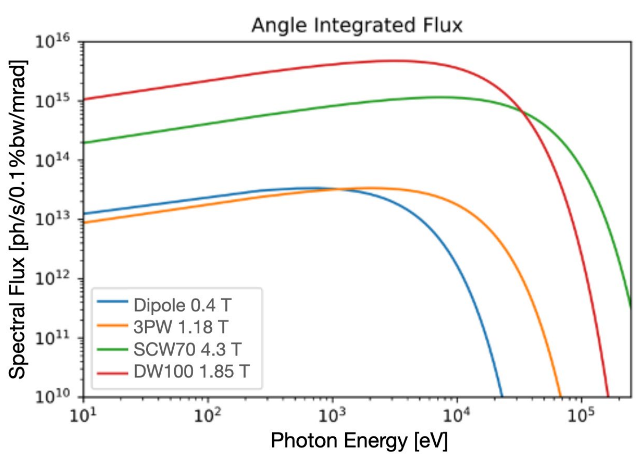


Figure 7: 3PW photon spectral flux integrated over the vertical angle.

The comparison between the photon flux emitted by the 3PW and a 0.4 T dipole shows that there is no absolute change to the total number photons emitted, just a shift in wavelength towards the higher photon energy. The radiation spectrum from the 3PW is similar in nature to that of the BM, but it extends to higher energies due to the higher peak field. Radiation from the 3PW covers the higher energy region beyond the practical upper limit of the conventional 0.4 T BM. At that limit, the photon flux of the 3PW is about a few hundred times greater than that of the dipole. Hence, the 3PW gives a larger flux at the high photon energy end of the spectrum than is normally available. Therefore, they are an alternate source of high energy X-rays for the existing bending magnet beamlines at the NSLS-II. The brightness provided by the 3PW sources is more than an order of magnitude higher than that of the NSLS-II bending magnets as illustrated in Tab. 3. Flux is in units of photons/s/0.1%bw/mrad and brightness is in units of photons /s/0.1%bw/$mm^2$/$mrad^2$. The spectral flux density for higher energies at 30 m far from the source is shown in Fig. 8 and the power density in Fig. 9.

Table 3: Comparison between NSLS-II BM and 3PW.

| | **NSLS-II BM** | | **NSLS-II 3PW** | |
|---|---|---|---|---|
| Energy | Flux [ph/s/0.1%bw/mrad] | Brightness [ph/s/0.1%bw/$mm^2$/mrad]$^2$ | Flux [ph/s/0.1%bw/mrad] | Brightness [ph/s/0.1%bw/$mm^2$/mrad]$^2$ |
| 10 eV | $1.25 \times 10^{13}$ | $4.04 \times 10^{14}$ | $8.8 \times 10^{12}$ | $1.97 \times 10^{14}$ |
| 100 eV | $2.5 \times 10^{13}$ | $1.85 \times 10^{15}$ | $1.8 \times 10^{13}$ | $9.10 \times 10^{14}$ |
| 1 keV | $3.3 \times 10^{13}$ | $6.84 \times 10^{15}$ | $3.2 \times 10^{13}$ | $3.98 \times 10^{15}$ |
| 10 keV | $1.7 \times 10^{12}$ | $1.17 \times 10^{15}$ | $1.8 \times 10^{13}$ | $6.93 \times 10^{15}$ |
| 50 keV | $1.9 \times 10^{5}$ | $3.05 \times 10^{8}$ | $1.1 \times 10^{11}$ | $1.05 \times 10^{15}$ |

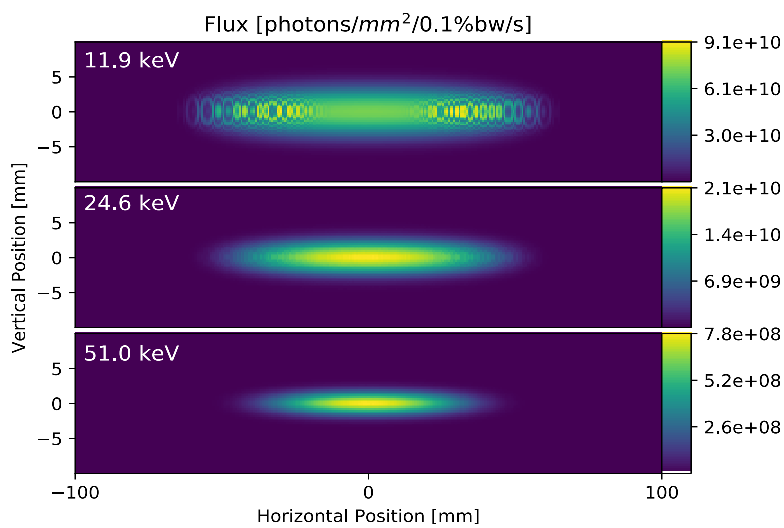


Figure 8: 3PW spectral flux density calculated for higher energies at a distance of 30 m from the source center.

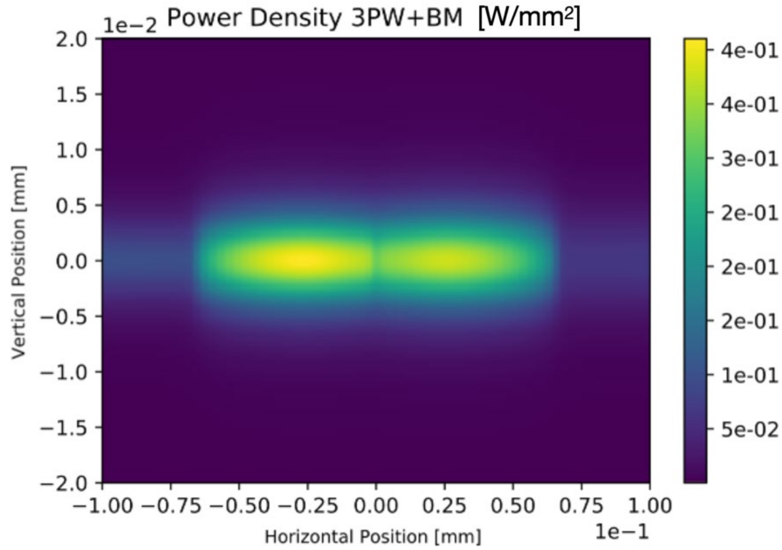


Figure 9: Power density of 3PW calculated including BM radiation from central part and edge.

We have successfully commissioned all 3PWs with the electron beam. The results of the beam commissioning for the 3PW located in cell 17 in the NSLS-II storage ring are described in detail.

The 3PW was slowly inserted from its extracted position of about $x$ = -190 mm to the fully inserted position of 0 mm, with an electron beam current of approximately 4 mA stored in the storage ring in the "bare lattice" mode, where all the other insertion devices are fully opened to prevent a beam dump from active interlock. During this motion, the beam orbit was significantly distorted from the nominal operation orbit as shown in Fig. 10, but there was no beam loss.

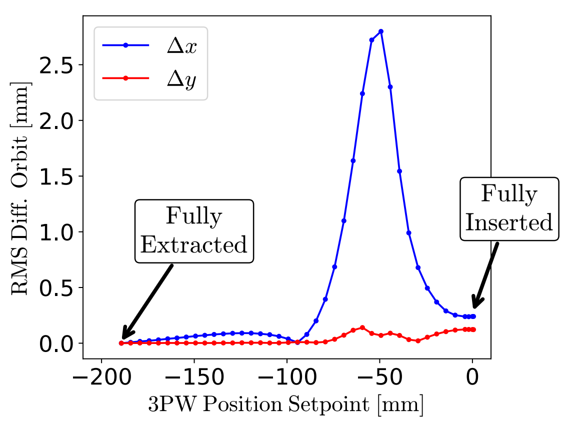


Figure 10: RMS orbit difference with respect to the orbit with 3PW extracted while inserting 3PW at Cell 17.

Figures 11 and 12, respectively, show the first and second field integrals of the 3PW estimated from the measured beam orbit distortion. The horizontal component of the first field integral is denoted as $I_{1x}$ and $I_{2x}$ for the second field integral. The vertical component is indicated as $I_{1y}$ and $I_{2y}$ for the first field and the second field integral, respectively. Using a lattice/particle tracking code called Tracy [14], the horizontal and vertical thin virtual kick elements at both the upstream and downstream ends of the 3PW element in a simulated lattice model were adjusted until the simulated orbit distortion fit the measured orbit distortion. The beam-based field integral estimates $I_1$ and $I_2$ were calculated from these best-fit kick angles, $\theta_{\mathrm{US}}$ for the upstream kick and $\theta_{\mathrm{DS}}$ for the downstream kick, using the following simple formula: $I_1 = B\rho(\theta_{\mathrm{US}} + \theta_{\mathrm{DS}})$ and $I_2 = B\rho \cdot L \cdot \theta_{\mathrm{US}}$, where $B\rho$ and $L$ are the magnetic rigidity and the length of the 3PW element, respectively. Figure 11 also contains the first field integrals of the 3PW measured by the flip-coil. The agreement between the beam-based and the flip-coil measurements is excellent, although there is a small discrepancy for $I_{1x}$ in the region $x > -30$ mm, which could be possibly explained if the beam orbit was vertically off center.

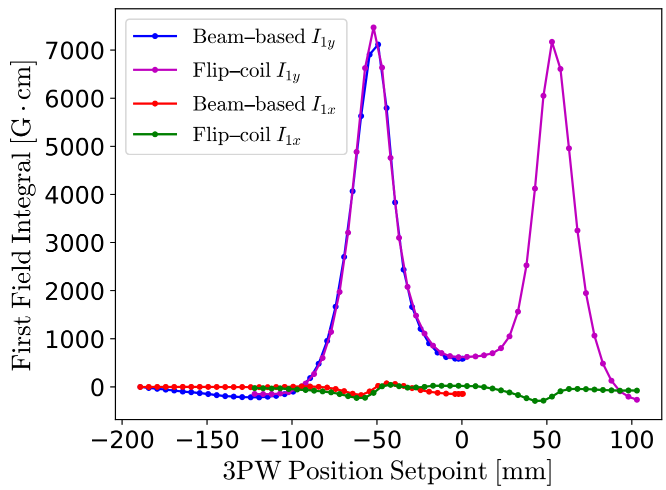


Figure 11: Comparison between the beam-based and flip-coil measurements of the 1st field integrals at Cell 17.

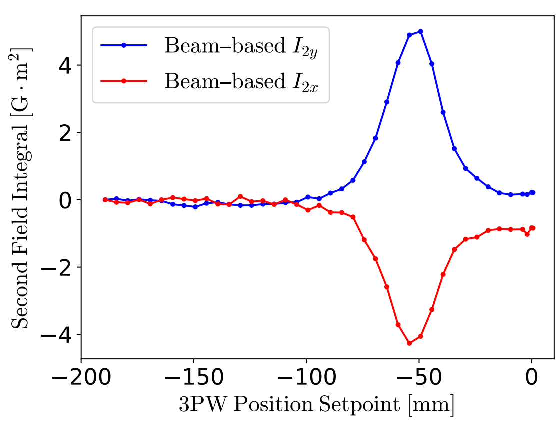


Figure 12: Beam-based measurement of 2nd field integrals for 3PW at Cell 17.

The residual orbit distortion was easily correctable by the slow orbit feedback. Finally, as expected, the insertion of the 3PW was confirmed to have negligible impact on other lattice and beam properties such as tunes, beta-beat, lifetime, and injection efficiency, for both the bare lattice and the operational lattice with three damping wigglers closed.

## 5. Conclusion

Three-pole wigglers have been constructed, optimized, installed, and successfully commissioned at NSLS-II storage ring. The magnetic properties of the devices have been investigated and found to satisfy the specification requirements as well as the electron and photon beam performances.


## Acknowledgment

This work was supported by the U.S. Department of Energy's Office of Science, under Contract No. DE-SC0012704.


## References


[1] T. Tanabe et al.,"Construction of Cryogen-Free 4.3T Superconducting Wiggler for NSLS-II Ring." IEEE Transactions on Applied Superconductivity 32, Issue 6. doi: Artn 410200 10.1109/Tasc.2022.3173248 (2022).

[2] T. Shaftan, J. Bengtsson and S. Kramer, "Control of Dynamic Aperture with Insertion Devices," Proceedings of the 10th European Particle Accelerator Conference, Edinburgh, Scotland, 2026, THPLS091.

[3] P. Ilinski, "NSLS-II X-Ray Diagnostics Development", Proceedings of 2011 Particle Accelerator Conference, New York, NY, USA, 2011, MOP199.

[4] J. Rank, NSLS-II Technical Note 221 (2016), https://technotes.bnl.gov/.

[5] M. Musardo, NSLS-II Technical Note 202 (2015). https://technotes.bnl.gov/.

[6] NSLS-II beamline map, https://www.bnl.gov/ps/nsls2/beamlines/map.php.

[7] Y. Hidaka, S. Krinsky, T. Tanabe, NSLS-II Technical Note 254 (2017) https://technotes.bnl.gov/.

[8] E.Hoyer et al., "Multiple Trim Magnets", Review of Scientific Instruments, Journal Volume: 66:2; Journal ID: ISSN 0034-6748, p.1902. USA (1995).

[9] O. Rudenko et al., "An Evolutionary Approach to Shimming Undulator Magnets for Synchrotron Radiation Sources", Lecture Notes in Computer Science, Volume 4193, doi:10.1007/11844297_37, January 2006.

[10] T. Tanabe et al., "Latest experiences and future plans on NSLS-II insertion devices", Proceedings of the 12th International Conference on Synchrotron Radiation Instrumentation, ISBN: 978-3-95450-168-7, New York, USA, Volume 1741, (2016).

[11] M. Musardo et al., "Magnetic Measurements of the NSLS- II Insertion Devices", Proceedings of the 6th International Particle Accelerator Conference, Richmond, Virginia, USA, May 3-8, 2015.

[12] M. Musardo et al., "NSLS-II Magnetic Measurement System Facility", Proceedings of the North American Particle Accelerator Conference, 2013, Pasadena, CA, USA, THPAC15.

[13] Open source code for advanced radiation simulation, http://oscars.bnl.gov/index.php

[14] J. Bengtsson, E. Forest, and H. Nishimura, "Tracy User Manual", Internal SLS document, PSI, Villigen (1997).